





Misfit-generated structural and optical anisotropies of the natural MoS₂-PbS van der Waals heterostructure merelaniite

Luca Bindi ^{1,*}, Arindam Dasgupta,² Pinaki Mukherjee ^{3,†}, Jie Gao,^{2,4} Xiaodong Yang ^{2,‡} and John A. Jaszczak ^{5,6,§}

¹*Dipartimento di Scienze della Terra, Università di Firenze, I-50121 Firenze, Italy*

²*Department of Mechanical and Aerospace Engineering, Missouri University of Science and Technology, Rolla, Missouri 65409, USA*

³*Department of Materials Science and Engineering, Michigan Technological University, 1400 Townsend Dr., Houghton, Michigan 49931, USA*

⁴*Department of Mechanical Engineering, Stony Brook University, Stony Brook, New York 11794, USA*

⁵*Department of Physics, Michigan Technological University, 1400 Townsend Dr., Houghton, Michigan 49931, USA*

⁶*A. E. Seaman Mineral Museum, Michigan Technological University, 1400 Townsend Dr., Houghton, Michigan 49931, USA*



(Received 11 June 2022; revised 16 August 2022; accepted 18 October 2022; published 10 November 2022)

Significant efforts developing MoS₂-PbS-based heterostructure devices with several different architectures show promise for photosensor, solar cell, and chemical sensor applications. Merelaniite (Mo₄Pb₄VSb₁₅) is a newly discovered natural van der Waals heterostructure of the cylindrite type, composed predominantly of heavily modulated pseudotetragonal PbS layers and pseudo-hexagonal MoS₂ layers with large misfit-induced anisotropy. For an incommensurate modulated structure, the refined structural model from single-crystal x-ray diffraction analysis is in reasonable agreement with the results obtained by high-resolution scanning transmission electron microscopy, especially in light of the fact that the two isolated single-crystal domains used for the x-ray and electron diffraction experiments were extracted from two different whiskers and subjected to different sample preparation methods. The effects of the misfit-induced structural anisotropy are studied using angle-resolved polarized Raman spectroscopy. The intensities of 12 Raman modes are studied as a function of incident polarization angle relative to merelaniite's whisker axis, and show maximal intensity with the polarization direction perpendicular to the whisker axis. Polarization-dependent anisotropic third-harmonic generation from ultrathin mechanically exfoliated flakes reveals the anisotropy of the third-order nonlinear susceptibility tensor. Merelaniite demonstrates an expanded structure-chemistry space for engineering stable layered materials for potential device applications.

DOI: [10.1103/PhysRevMaterials.6.115202](https://doi.org/10.1103/PhysRevMaterials.6.115202)

I. INTRODUCTION

The ability to control the structure of materials and thereby to tailor their properties has long been the goal of materials scientists and engineers. Following the discovery of graphene, vertically stacked van der Waals (vdW) heterostructures have provided a vast space for exploration and utilization of new chemistries and structures for materials design [1]. While tremendous advances have been made in fabricating such heterostructures amid challenges presented by issues of stability, naturally occurring minerals that are layered vdW heterostructures provide another route to studying such complex materials [2,3]. In particular, the structural, electronic, optical, optoelectronic, and electrocatalytic properties

of several minerals, including franckeite [4–9], cylindrite [10], lengenbachite [11], teallite [7,12], and others have been studied in systems ranging from bulk down to just a few layers.

Besides graphene, few-layer and monolayer transition-metal dichalcogenides, especially MoS₂, have been some of the most intensely studied 2D materials for a wide variety of potential electronic, optical, and optoelectronic applications [13–16]. In MoS₂, the Mo atoms typically have trigonal-prismatic coordination with the S atoms, and exhibit a band-gap transition from indirect in bulk- and few-layer materials to direct for the monolayer material. Monolayer MoS₂ also exists in a metastable structure with distorted octahedral coordination and tetragonal symmetry (1T-MoS₂). In contrast to the trigonal-prismatic coordination structures, which are semiconducting, the octahedrally coordinated 1T-MoS₂ is metallic [17,18]. Furthermore, bulk 1T-MoS₂ crystals have been observed [19] to become superconducting below a critical temperature of 4 K. The stability of 1T-MoS₂ is sensitive to aging, temperature, and importantly in the context of fabricating heterostructures, the interaction of the monolayer with substrates [17,19,20].

Looking beyond pure MoS₂, MoS₂-PbS-based heterostructure devices with several different architectures, typically employing layered MoS₂ and PbS quantum dots, have been studied and show promising photoresponse and

*luca.bindi@unifi.it

†Present address: Stanford Nano Shared Facilities, Stanford University, 348 Via Pueblo, Stanford, CA 94305.

‡yangxia@mst.edu

§jaszczak@mtu.edu

Published by the American Physical Society under the terms of the [Creative Commons Attribution 4.0 International](https://creativecommons.org/licenses/by/4.0/) license. Further distribution of this work must maintain attribution to the author(s) and the published article's title, journal citation, and DOI.

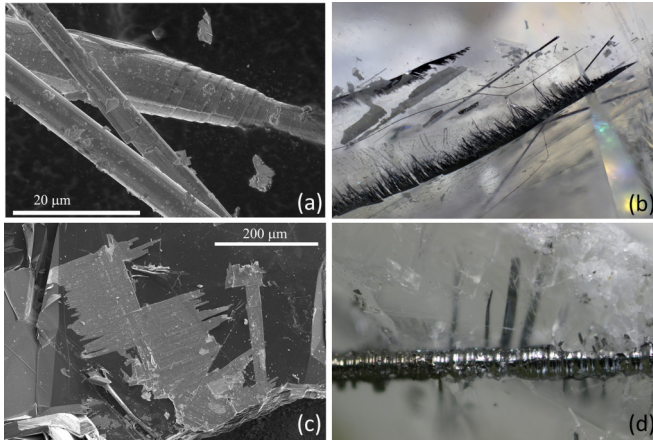


FIG. 1. Morphology of merelaniite. (a) SEM image of merelaniite whiskers showing the circumferentially wound layers. (b) Cylindrical whiskers and comblike thin layers of merelaniite enclosed in calcite (8.75-mm-wide field of view). (c) SEM image of flat merelaniite layers on the (001) surface of a graphite crystal. (d) A 1.4-mm-long section of cylindrical merelaniite in calcite with attached partially nonwound thin merelaniite layers. The sample shown in (d) is in the Natural History Museum (London) collection, no. BM2017,111).

detectivity for infrared photosensor applications [13,21–26]. For solar-cell applications, MoS₂ layers have been shown to be an effective hole-transport material in combination with light-absorbing PbS quantum dots [27]. Optoelectronic devices fabricated with nanoplate PbS grown on few-layer MoS₂ have demonstrated nonvolatile optical memory characteristics with infrared pulses [28]. High surface area MoS₂ clusters modified with PbS quantum dots have shown enhanced performance as a NO₂ detector over MoS₂ clusters alone [29].

Among naturally occurring vdW materials [2], merelaniite (Mo₄Pb₄VSbS₁₅) is the newest member of the family of misfit-layer sulfosalts of the cylindrite structure type, but is composed primarily of alternating MoS₂ and PbS layers [30]. The new mineral is found as fine cylindrical whiskers of circumferentially wound layers [Fig. 1(a)] that can be associated with graphite, alabandite, zoisite (variety tanzanite), prehnite, quartz, calcite, and other minerals from the tanzanite gem mines near Merelani, Lelatema Mountains, Manyara Region, Tanzania. Rarely, it also occurs as nonwound thin sheets [Figs. 1(b)–1(c)], which are sometimes attached to cylindrical whiskers [Fig. 1(d)]. To date, the Merelani tanzanite mines are the only confirmed locality for merelaniite.

Merelaniite is unique among related misfit-layer compounds in regard to its semicomensurability along the modulation direction. The *H* and *Q* lattice parameters along that direction (b_H and b_Q , respectively) have been observed [31,32] to be in the ratio of two successive integers (Vernier principle) such that $b_H/b_Q \approx (n+1)/n \equiv n_Q/n_H$, with corresponding ratios, for example, $n_Q/n_H = 13/12$ for cylindrite and lévyclaudite, 12/11 for Sn²⁺-rich franckeite, 16/15 for Sn²⁺-free franckeite, and 14/13 for lévyclaudite-(Sb). On the other hand, with $n_Q/n_H = 13/14$, merelaniite is unique having $n_Q < n_H$, due to its relatively small *H*-layer lattice parameter.

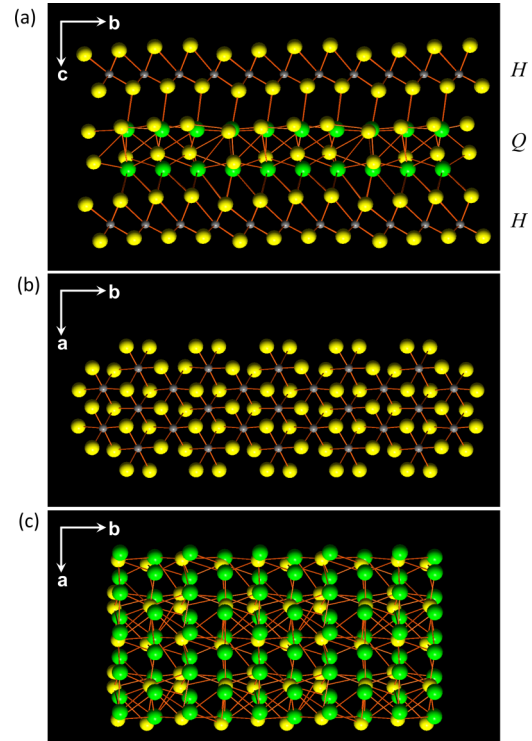


FIG. 2. Crystal structure of merelaniite. (a) View as seen down [100] with \mathbf{a}_{13}^* vertical. (b) The *H* layer as seen down [001]. (c) The *Q* layer as seen down [001]. Green, gray, and yellow circles refer to Pb, Mo, and S atoms, respectively.

In this study we present the crystal structure of merelaniite, as determined from single-crystal x-ray diffraction, demonstrating large modulations in bond distances and atomic positions along the modulation direction \mathbf{q} , with consistent results from high-resolution scanning transmission electron microscopy (STEM) data. X-ray photoelectron spectroscopy (XPS) was used to study the oxidation states of the primary elements. The large in-plane structural anisotropy of merelaniite was probed by angle-resolved polarized Raman spectroscopy. We also demonstrate that merelaniite crystals can be mechanically exfoliated down to a thickness of 8 nm, corresponding to only around seven layer pairs of the heterostructure. By performing polarization-dependent third-harmonic generation (THG) measurements, the anisotropic nonlinear optical response from the exfoliated merelaniite thin flakes is demonstrated, and the third-order nonlinear susceptibility of merelaniite crystal is estimated.

II. RESULTS AND DISCUSSION

A. Crystal structure

The structure of merelaniite has been determined by single-crystal x-ray diffraction on the basis of the (3 + 2)-dimensional superspace approach (see Ref. [3] for a review). This misfit-layer compound, of the cylindrite type, results from the combination of two heavily modulated *C*-centered triclinic *H* and *Q* subsystems (Fig. 2). The *Q* pseudotetragonal layer can be described as derived from the NaCl archetype, while the *H* pseudo-hexagonal layer was derived from the CdI₂

TABLE I. Refined crystallographic data for merelaniite.

<i>H</i> layer (first index = 1)	
a_{11}, a_{12}, a_{13} (Å)	3.156(7), 5.547(8), 11.910(10)
$\alpha_1, \beta_1, \gamma_1$ (°)	92.13(10), 89.52(10), 90.18(10)
V_1 (Å ³)	208(2)
<i>Q</i> layer (first index = 2)	
a_{21}, a_{22}, a_{23} (Å)	5.929(8), 5.961(5), 12.030(10)
$\alpha_2, \beta_2, \gamma_2$ (°)	91.33(9), 90.88(5), 91.79(4)
V_2 (Å ³)	425(2)
Wave vectors	
\mathbf{q}_{11}	$0.00322(7)\mathbf{a}_{11}^* + 0.15255(16)\mathbf{a}_{12}^* - 0.01359(5)\mathbf{a}_{13}^*$
\mathbf{q}_{12}	$0.63088(9)\mathbf{a}_{11}^* + 1.0737(11)\mathbf{a}_{12}^* - 0.44367(5)\mathbf{a}_{13}^*$

archetype. The modulations along \mathbf{q}_{11} are readily apparent, as illustrated in Fig. 2(a). Refined crystallographic parameters [33] are summarized in Table I.

A thorough analysis of the reflection distribution revealed the two misfit subsystem cell orientations: the overall pattern can be interpreted as the combination of two heavily (i.e., with satellites up to third order) modulated triclinic subsystems with a common incommensurate \mathbf{q} wave vector ($\mathbf{q}_{11} = \mathbf{q}_{21}$) and only one shared reciprocal axis ($\mathbf{a}_{13}^* = \mathbf{a}_{23}^*$). Thus, all the reflections were indexed with six integer indices, and the structure was refined starting from the atomic coordinates reported for lévyclaudite [32] using the program JANA2006 [34]. Details of the embedding of reflections in superspace can be found in Ref. [32]. Unfortunately, the number of independent reflections did not allow us to refine the occupancy of the site positions of the two layers. We therefore constrained the metal atom positions in the *H* and the *Q* subsystems as fully occupied by Mo and Pb, respectively, neglecting the minor but significant amounts [30] of V and Sb. In the final stage, the refinement converged to $R = 0.0419$ ($wR = 0.0498$) for 33 794 (6728 main reflections and 27 066 satellite reflections) independent reflections (3σ level) and 157 parameters.

Within the *H* layer, Mo atoms occupy octahedral sites [Fig. 2(b)], with Mo-S distances varying along both the longitudinal and the transverse wave directions. The Mo-S distances [2.430(8) Å on average] are close to that observed in hexagonal molybdenite (2.366 Å) by Schonfeld *et al.* [35], and even closer to that observed in bulk 1T-MoS₂ [2.389(5) Å] by Fang *et al.* [19]. The Mo-S distances vary from 1.94 to 3.07 Å in the structure, which could be symptomatic of different valence states for Mo (see XPS results below)—and likely different coordinations—in different portions of the modulated structure, as is made evident by the calculation of the bond valence through the modulated structure [Fig. 3(a)] as a function of the phase coordinate t along the fourth reciprocal superspace vector (whose real-space projection is \mathbf{q}_{11}) [32,36]. Alternatively, the strong variation of the Mo-S distances could be related to a Mo-for-V substitution, as is indicated by the STEM data (see below).

In the *Q* layer, resembling a two-atom-thick slice of a NaCl-type structure, the Pb atoms are on the outside of the corrugated layer [Fig. 2(c)] and may therefore make possible bonding interactions with the S atoms of the adjacent *H* layer. Each metal atom is then coordinated to five S atoms within the *Q* layer and to one or two S atoms in the neighboring

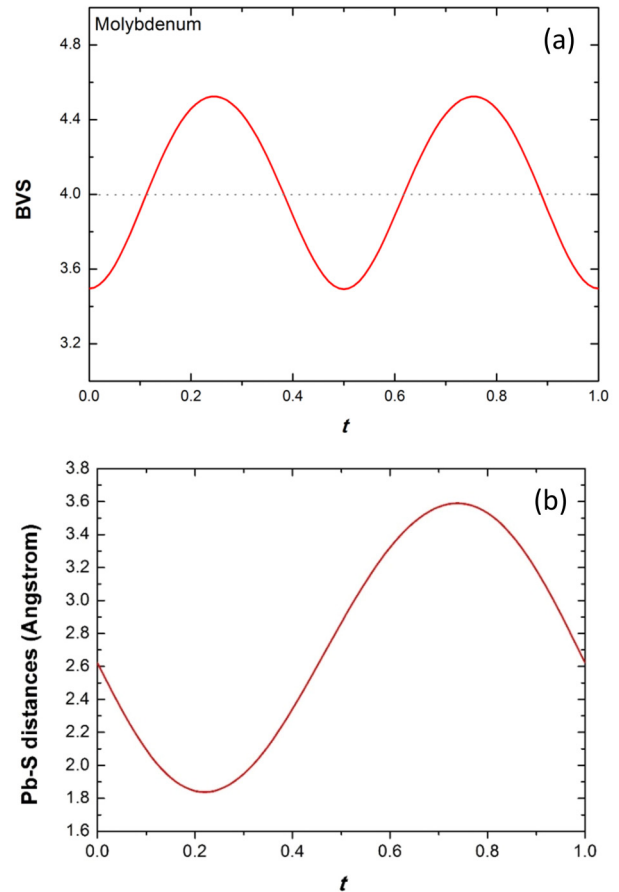


FIG. 3. Structure modulations. (a) Variation of the bond-valence sums (BVS) of Mo as a function of the fourth coordinate (t) in the superspace in the *H* layer of the merelaniite structure. (b) Variation of the Pb-S bond distances as a function of the fourth coordinate (t) in the superspace in the *Q* layer of the merelaniite structure.

H layer. The Pb-S bond distance is 2.869(5) Å on average, with variations of ± 0.9 Å along the internal t superspace coordinate. It is remarkable to observe such a large dispersion of the bond distances as a function of t [Fig. 3(b)], in accord with the huge displacement of the atoms perpendicular to the layers (Δz of the Pb position ranging from -0.64 to 0.65 Å). It is noteworthy that a similar displacement of atoms was observed in lévyclaudite [32], with Δz of the Sn position ranging from ~ -0.75 to 0.75 Å; however, this produced only a small dispersion of the Sn-S bond distances.

Figure 4(a) shows a high-angle annular dark-field (HAADF) STEM image of a merelaniite crystal projected along the [100] zone axis. The contrast in HAADF STEM images is proportional to $Z^{2-\delta}$, where Z is the atomic number and δ is an instrument factor that depends on the HAADF detector geometry [37,38]. In this image, the brightest contrast comes from Pb atoms followed by Mo atoms. Figure 4(b) shows a magnified section of Fig. 4(a), with a portion of the refined modulated structure model superimposed onto the STEM image projected along the same zone axis (with Pb, Mo, and S atoms shown in green, gray, and yellow spheres, respectively). Considering that there are strains induced by the bend that is visible at the top right of Fig. 4(a), and the fact

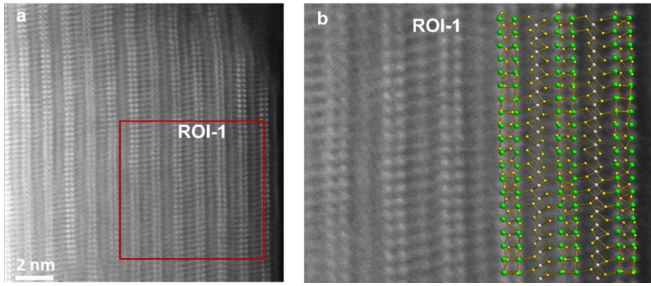


FIG. 4. Atomic resolution imaging of merelaniite. (a) HAADF-STEM image of a merelaniite crystal projected along [100] zone axis. In this mode, brighter contrast comes from elements with higher atomic number. Here, the brightest columns consist of Pb atoms, and the less-bright columns consist of Mo atoms. A bend in the sample is visible at the top right. The section outlined in red is presented at higher magnification in (b) with the refined structure model projected on it. Pb, Mo, and S atoms are shown in green, gray, and yellow spheres, respectively.

that the structure is incommensurate, which leads to a lack of periodicity in real space, there is reasonably good agreement between the STEM image and the refined structure model. The differences visible in Fig. 4(b) may also be related to the fact that the two isolated single-crystal domains used for the x-ray and electron diffraction experiments, which were extracted from two different whiskers, may not be precisely representative of the same bulk. Indeed, natural materials (i.e., minerals) can show subtle chemical variations responsible for minor structural deviations and disorder, even within a single-crystal domain. Additionally, some shearing may possibly have taken place in the ultramicrotome preparation of the TEM foil, which could also account for some of the observed differences with the refined structure model, such as differences in some of the Pb/S atom positions normal to the stacking direction, within the *Q* layers shown in Fig. 4(b). A solution to the problem could be the application of a total scattering technique such as the atomic pair-distribution function analysis of powder-diffraction data (e.g., Ref. [39]). Unfortunately, the paucity of available material and the chemical inhomogeneity precluded such investigation.

To confirm the atom positions within the crystal structure, we further have performed energy-dispersive x-ray spec-

troscopy mapping at the atomic scale. Overall composition in atomic fraction (at. %) obtained from nine areas are as follows: Mo 17.5(±3.5), Pb 14.8(±1.3), V 4.0(±0.4), Sb 1.7(±0.3), and S 62.0(±4.9). Figure 5(a) shows an energy-dispersive spectroscopy (EDS) x-ray map where the HAADF image is superimposed with x-ray maps of Pb, Mo, and S, respectively, as well as the maps of these individual atoms. The corresponding line-scan plot is shown in Fig. 5(b). As observed from Fig. 4, the Pb-atom positions coincide with the HAADF signal and Mo atom positions are out of phase with the Pb atom positions. The peaks of S-atom positions are quite broad and partly coincide with both Pb and Mo atoms. We investigated another area with the same EDS measurements (cf. Supplemental Material, Fig. S1 [33]). There, along with the similar trends with Pb, Mo, and S atoms, we have found that the V-atom positions anticorrelate with Pb-atom positions, and partly coincide with the Mo- and S-atom positions.

Next, XPS was performed on merelaniite flakes to determine the surface chemical composition and the oxidation states of the elements. According to the XPS spectra, the main elements of Mo, Pb, and S are present, whereas V and Sb are not apparently observed. Figure 6 shows the high-resolution XPS spectra at the binding-energy regions of Mo 3*d*, Pb 4*f*, and S 2*p*, where the peak fittings are used to determine the oxidation states of individual elements. Results indicate that lead is present in the material in Pb²⁺ (88%) and Pb⁴⁺ (12%) oxidation states, which is the same as that found for Pb in cylindrite [10] and very similar for lengenbachite (91% Pb²⁺ and 9% Pb⁴⁺) [11]. Molybdenum is present in the material in Mo⁴⁺ (91%) and Mo⁶⁺ (9%) oxidation states, while sulfur was found to be exclusively present as S²⁻.

B. Studying structural anisotropy with Raman spectroscopy

As illustrated in the inset of Fig. 7(a), the Raman spectra from the top surface area of a bulk merelaniite cylinder (spot 1) and the connected unrolled flat area (spot 2) are collected and analyzed. It is found that the Raman spectra from these two spots are almost the same (Fig. S2 [33]), indicating that the crystal structure remains the same as the merelaniite cylinder is unrolled into the flat flake. Figure 7(a) shows the measured Raman spectrum from the top

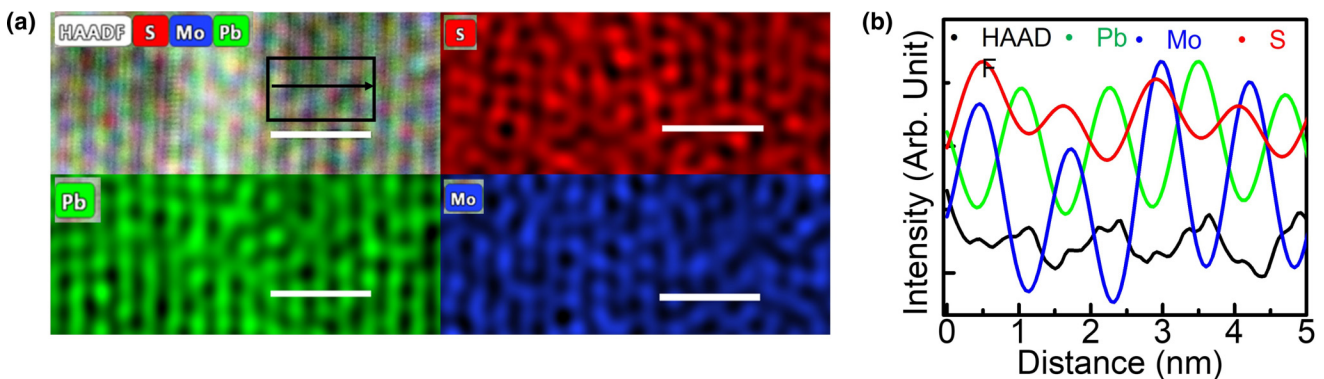


FIG. 5. Atomic resolution chemical mapping of merelaniite. (a) Atomic-resolution EDS x-ray maps of Pb, Mo, S, and all three superimposed on HAADF-STEM image of a merelaniite crystal projected along [100] zone axis. Scale is 5 nm. (b) Line profiles of the atoms from the boxed area shown in (a).

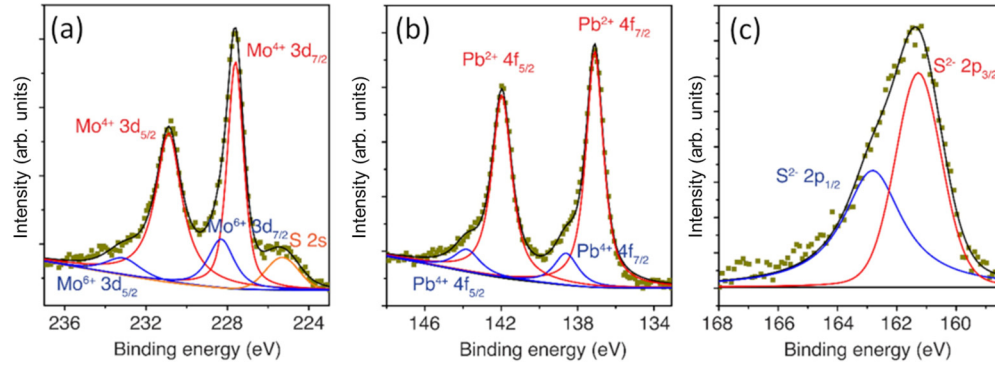


FIG. 6. High-resolution XPS spectra around the respective binding energy regions of (a) Mo 3d, S 2s, (b) Pb 4f, and (c) S 2p.

surface area of cylinder with a 632.8-nm He-Ne laser as the excitation source in parallel polarization configuration, where the analyzer direction is set to be parallel to the incident linear polarization direction. The Raman spectrum of merelaniite exhibits several distinct Raman peaks within the spectral range of 100–850 cm^{-1} , which are located at 122, 142, 163, 189, 215, 230, 286, 326, 354, 383, 392, 404, 459, 611, and 777 cm^{-1} . The Raman modes of merelaniite can be assigned according to the Raman spectra of the component binary sulfides, including molybdenite MoS_2 [16,40], galena PbS [41], stibnite Sb_2S_3 [42,43], and vanadium disulfide VS_2 [44,45]. The peaks at 122 and 142 cm^{-1} are assigned as the two-phonon process modes of VS_2 (121 and 150 cm^{-1}). The 163- cm^{-1} peak represents a combination of the A_g mode of Sb_2S_3 (156 cm^{-1}) and the two-phonon process mode of VS_2 (168 cm^{-1}). The 189- cm^{-1} peak is assigned as the A_g mode of Sb_2S_3 (191 cm^{-1}). The peak at 215 cm^{-1} corresponds to the longitudinal optical phonon modes of PbS (204 cm^{-1}). The 230- cm^{-1} peak is assigned as the B_{1g}/B_{3g} mode of Sb_2S_3 (238 cm^{-1}). The 286- cm^{-1} peak is attributed to the A_g mode of Sb_2S_3 (283 cm^{-1}), as well as the E_{1g} mode arising from the octahedral coordination of Mo atoms in $1T$ - MoS_2 [17,19,20,46]. We note that $1T$ - MoS_2 with distorted octahedral coordination also has three additional Raman bands (J_1 at 150–156 cm^{-1} , J_2 at 212–226 cm^{-1} , and J_3 at 324–333 cm^{-1}) that are thought to arise from superlattice zone folding, and may contribute to respective Raman bands in merelaniite [17,20,46]. The 326- cm^{-1} peak represents the A_{1g} out-of-plane vibration mode of VS_2 (325 cm^{-1}) and the peak at 354 cm^{-1} is attributed to one Raman mode of VS_2 (360 cm^{-1}). The peaks at 383 and 392 cm^{-1} are attributed to the E_{2g} in-plane vibration mode of MoS_2 (384 cm^{-1}). The prominent Raman peak at 404 cm^{-1} is assigned as the A_{1g} out-of-plane vibration mode of MoS_2 (409 cm^{-1}). The 459- cm^{-1} peak is related to the first overtone of the longitudinal optical phonons of PbS (454 cm^{-1}) and the second-order $2LA(M)$ mode due to longitudinal acoustic phonons of MoS_2 (450 cm^{-1}). Finally, the broad Raman shifts about 611 and 777 cm^{-1} are related to the first-order and second-order Raman modes due to the resonant Raman scattering in MoS_2 (572, 600, 643 cm^{-1} and 756, 782, 820 cm^{-1} , respectively).

Furthermore, angle-resolved polarized Raman spectroscopy is conducted to study the structural anisotropy and identify the crystal axes of merelaniite. Figure 7(b) displays

the Raman intensity contour map depending on the incident linear polarization angle, taken from the top surface area of merelaniite cylinder in the parallel polarization configuration, indicating the polarization-sensitive periodic variations of Raman mode intensities. Figures 7(c)–7(n) show the polar plots of the Raman A_g modes at 142, 163, 189, 215, 230, 286, 326, 354, 383, 392, 404, and 459 cm^{-1} measured in parallel polarization configuration as a function of the incident linear polarization angle θ . By considering only the in-plane components of the electric field, the Raman tensor of a given A_g mode for the triclinic merelaniite crystal is written as $R = \begin{pmatrix} u & w \\ w & v \end{pmatrix}$, where u , v , and w are the components of the Raman tensor. The Raman intensity of the A_g mode in parallel configuration can be written as [47]

$$I_{A_g}^{\parallel}(\theta) \propto (ucos^2\theta + 2w \sin\theta \cos\theta + vsin^2\theta)^2. \quad (1)$$

As shown in Figs. 7(c)–7(n), the measured data agree well with the theoretical fits to Eq. (1). Similar to results for other naturally occurring incommensurate vdW heterostructures franckeite [9], cylindrite [10], and lengenbachite [11], the in-plane structural anisotropy leads to anisotropic twofold patterns in the polar plots of Raman intensity in parallel polarization configuration as a function of incident polarization angle for all of the examined modes (Fig. 7). As observed for cylindrite and franckeite, the intensities for merelaniite reach primary maxima at 0° and 180° along the $\pm x$ direction for all modes. Secondary maxima are pronounced along the $\pm y$ direction for all four of the examined Raman modes for cylindrite, whereas secondary maxima along the $\pm y$ direction are observed for only 2 of 12 studied modes in merelaniite, and are much less prominent than the primary maxima [Figs. 7(f) and 7(h)]. Secondary maxima are also absent or very weak along the $\pm y$ direction for franckeite. On the other hand, depending on the mode studied, primary maxima for lengenbachite can occur along either the $\pm x$ - or $\pm y$ -directions, with secondary maxima evident for most of the studied modes.

Polarization-resolved Raman scattering in parallel polarization configuration has been used to infer the directions of the in-plane crystal axes and modulation directions in franckeite [9], cylindrite [10], and lengenbachite [11]. Since, in the present study, the x direction ($\theta = 0^\circ$) was experimentally set up to be perpendicular to the axial direction of the merelaniite cylinder, the above results indicate that the modulation

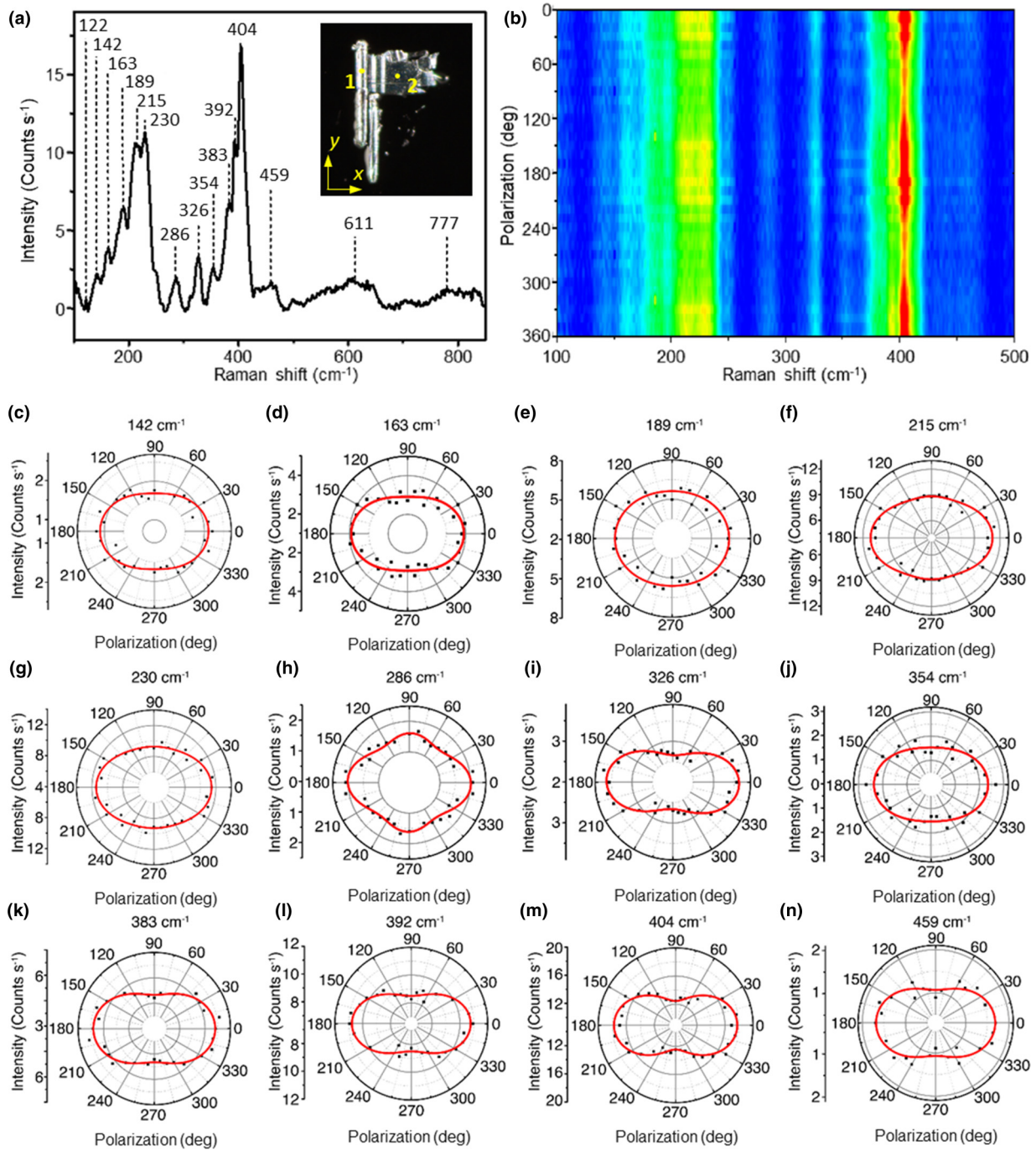


FIG. 7. Anisotropic Raman scattering from merelaniite crystal. (a) Recorded Raman spectrum from the top surface area of merelaniite cylinder (spot 1) in parallel polarization configuration, where the observed Raman peaks are labeled. (b) Contour map of the angle-resolved polarized Raman spectra obtained in parallel polarization configuration. (c)–(n) Polar plots for different Raman modes at 142, 163, 189, 215, 230, 286, 326, 354, 383, 392, 404, and 459 cm^{-1} . The measured values are indicated with black points, while the theoretical fits are shown with red solid curves.

direction \mathbf{q}_{11} of the merelaniite crystal is either along the cylinder axis ($\pm y$ direction) or normal to it ($\pm x$ direction) in the plane of the layers. However, since in the case of lengenbachite it was shown by complimentary TEM studies that the modulation direction can be along the direction of the primary maxima or along the direction of the secondary maxima, depending on the Raman mode examined [11], the orientation

of the modulation direction relative to the cylinder axis for merelaniite is not determined unambiguously. Nevertheless, this is consistent with prior studies that have shown that in cylindrite, the modulation vector is parallel to the cylinder axis [48,49].

According to Eq. (1), the Raman intensity ratio $I_{A_g}^{\parallel}(\theta = 0^\circ)/I_{A_g}^{\parallel}(\theta = 90^\circ)$ underlines the anisotropy ratio of

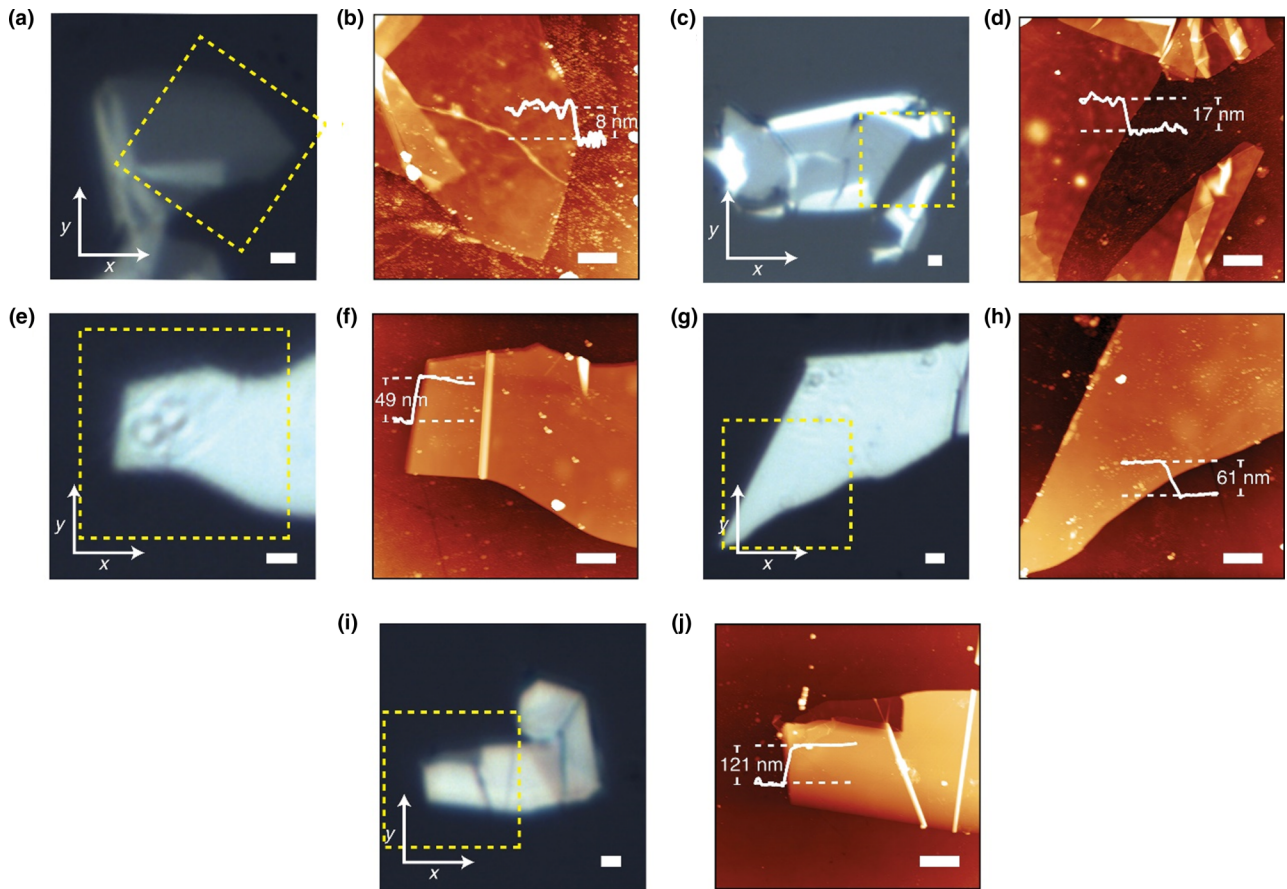


FIG. 8. Mechanical exfoliation of merelaniite thin flakes. (a), (c), (e), (g), (i) Optical reflection microscope images of mechanically exfoliated merelaniite crystals with thicknesses of 8, 17, 49, 61, and 121 nm, respectively. The yellow dashed boxes indicate the scanned regions for AFM images. (b), (d), (f), (h), (j) Corresponding AFM images in the scanned regions. AFM line profiles confirm the thicknesses of the probed crystals. Scale bars are 2 μm .

Raman tensor $|u|^2/|v|^2$ in the merelaniite crystal. It is found that the ratios of $|u|^2/|v|^2$ are 1.265 for the 230-cm^{-1} mode and 1.424 for the 404-cm^{-1} mode from the top surface area of the cylinder (spot 1), whereas almost the same ratios of 1.297 and 1.487 are obtained for these two modes from the unrolled flat area (spot 2). This indicates that the structural anisotropy of the merelaniite crystal remains almost unchanged between the cylinder and the unrolled flake.

C. Mechanical exfoliation

The vdW-heterostructure nature of merelaniite crystal leads to weak interlayer interactions, which indicates the feasibility of obtaining thin flakes by mechanical exfoliation. Here, the bulk merelaniite crystal is mechanically exfoliated using Nitto tape (SPV 224) to get thin flakes with various thicknesses on a quartz substrate. Figure 8(a) shows the reflection optical microscope image of an isolated ultrathin merelaniite crystal on a quartz substrate. Figure 8(b) presents an atomic force microscope (AFM) image of the scanned region marked by the yellow dashed box in Fig. 8(a). The thickness of the flake is 8 nm according to the AFM line profile, indicating that the flake consists of only around seven layer pairs. In addition, Figs. 8(c), 8(e), 8(g), and 8(i) show

the reflection optical images of other exfoliated merelaniite flakes, where the associated AFM images in Figs. 8(d), 8(f), 8(h), and 8(j) demonstrate that the flake thicknesses are 17, 49, 61, and 121 nm, respectively.

D. Anisotropic nonlinear optical response

The effect of the in-plane structural anisotropy on the nonlinear optical response of merelaniite crystal was further investigated by measuring the polarization-dependent anisotropic THG emission. Figure 9(a) plots the recorded THG spectrum from the 8-nm-thick merelaniite flake showing an expected peak emission at the wavelength of 520 nm, which is exactly at one-third of the fundamental wavelength of 1560 nm. The inset of Fig. 9(a) shows the transmission optical microscope image with the green color emission. The log-scale plot of the THG power dependence on the fundamental laser power in Fig. 9(b) shows a cubic power law with the slope of 2.97 ± 0.04 , which further confirms the THG process. To determine the crystal axes of the probed exfoliated flakes, polarization-resolved Raman spectra are recorded. Figure 9(c) displays the polar plot of the Raman A_g mode at 190 cm^{-1} for the 8-nm-thick merelaniite flake, which indicates that the x direction ($\theta = 0^\circ$) is oriented normal to what

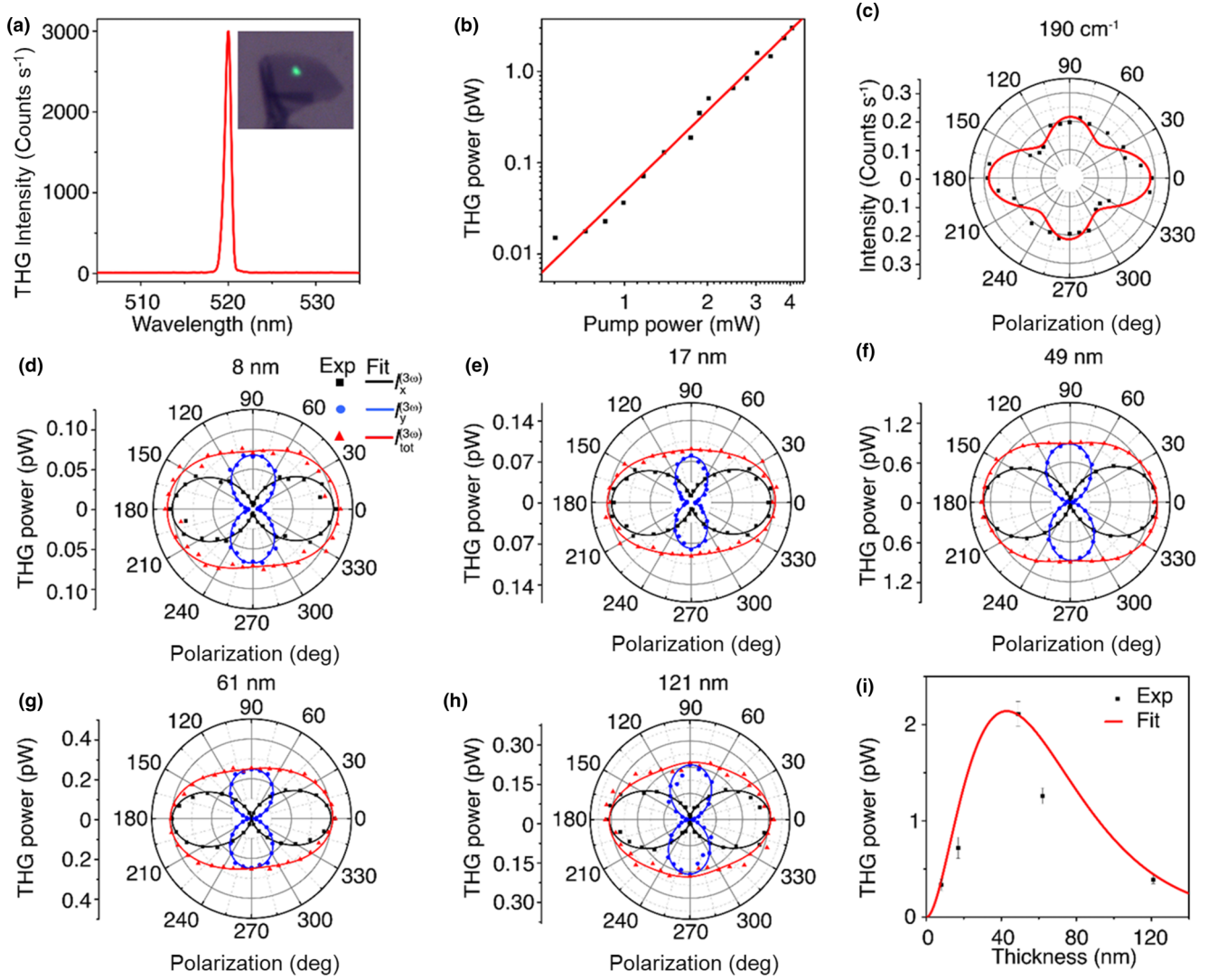


FIG. 9. Anisotropic THG emission from merelaniite thin flakes. (a) Recorded THG spectrum from the 8-nm-thick merelaniite flake, showing a peak emission at 520 nm. Inset shows the transmission optical image of the THG emission from the flake. (b) Log-scale plot of the measured average THG power as a function of the incident laser power. (c) Polar plot of the Raman A_g mode at 190 cm^{-1} for the 8-nm-thick merelaniite flake. (d)–(h) Angular evolution of the average THG emission power as a function of the incident pump-polarization angle for merelaniite flakes with thicknesses of 8, 17, 49, 61, and 121 nm. Black square ($I_x^{(3\omega)}$), blue circle ($I_y^{(3\omega)}$), and red triangle ($I_{\text{tot}}^{(3\omega)}$) data points are the measured data, while the solid curves are the corresponding theoretical fits. (i) Evolution of the average THG emission power vs the flake thickness.

would be the cylinder axis, consistent with the orientation of the sample in Fig. 7.

Next, anisotropic THG responses from the exfoliated merelaniite flakes are characterized. Considering that merelaniite belongs to the triclinic crystal system, the contracted form of the third-order nonlinear susceptibility tensor $\chi^{(3)}$ can be approximately expressed as [50]

$$\chi^{(3)} = \begin{pmatrix} \chi_{11} & \chi_{12} & \chi_{13} & \chi_{14} & \chi_{15} & \chi_{16} & \chi_{17} & \chi_{18} & \chi_{19} & \chi_{10} \\ \chi_{21} & \chi_{22} & \chi_{23} & \chi_{24} & \chi_{25} & \chi_{26} & \chi_{27} & \chi_{28} & \chi_{29} & \chi_{20} \\ \chi_{31} & \chi_{32} & \chi_{33} & \chi_{34} & \chi_{35} & \chi_{36} & \chi_{37} & \chi_{38} & \chi_{39} & \chi_{30} \end{pmatrix}, \quad (2)$$

where the first subscript 1, 2, 3 represents x, y, z respectively, and the second subscript refers to the following combination

of the three components as

$$\begin{matrix} xxx & yyy & zzz & yzz & yxz & xzz & xxz & xyy & xxy & xyz \\ 1 & 2 & 3 & 4 & 5 & 6 & 7 & 8 & 9 & 0 \end{matrix}$$

Now, if the electric field of the fundamental laser at frequency ω is polarized at an angle θ with respect to the x axis, then it can be written as $\vec{E}^{(\omega)} = E_0(\cos\theta \hat{x} + \sin\theta \hat{y})$, where \hat{x} and \hat{y} are the unit vectors along the x - and y -axes. Since the excitation electric-field polarization always remains in the x - y plane in our experimental configuration, no contribution from the components relating to the z terms of the $\chi^{(3)}$ tensor is

TABLE II. Comparison of third-harmonic generation properties of natural vdW materials.

	Relative magnitudes of the components of the third-order nonlinear susceptibility tensor	Estimated $\chi_{\text{eff}}^{(3)}$ ($10^{-19} \text{ m}^2 \text{ V}^{-2}$)
	$\chi_{11} : \chi_{12} : \chi_{18} : \chi_{19} : \chi_{21} : \chi_{22} : \chi_{28} : \chi_{29}$	
Merelaniite	1: 0.023: 0.326: 0.004: 0.012: 0.788: 0.006: 0.258	0.482
Cylindrite [10]	1: 0.012: 0.121: 0.016: 0.003: 0.663: 0.002: 0.107	3.06
Franckeite [9]	1: 0.012: 0.043: 0.015: 0.017: 0.815: 0.009: 0.037	1.87
Lengenbachite [11]	1: 0.03: 0.13: 0.02: 0.01: 0.72: 0.02: 0.11	2.18

expected in the THG signal. Therefore, the x - and y -polarized components of the resulting THG signal can be expressed as

$$I_x^{(3\omega)} \propto (\chi_{11} \cos^3 \theta + \chi_{12} \sin^3 \theta + 3\chi_{18} \cos \theta \sin^2 \theta + 3\chi_{19} \sin \theta \cos^2 \theta)^2, \quad (3)$$

$$I_y^{(3\omega)} \propto (\chi_{21} \cos^3 \theta + \chi_{22} \sin^3 \theta + 3\chi_{28} \cos \theta \sin^2 \theta + 3\chi_{29} \sin \theta \cos^2 \theta)^2. \quad (4)$$

The effect of the incident linear polarization angle on the THG emission power from the merelaniite thin flakes is then characterized. The desired linear polarization of the pump beam is obtained by placing a linear polarizer oriented along the x axis and a rotating half-wave plate. Figure 9(d) plots the angular dependence of the THG emission power as a function of the excitation linear polarization angle with respect to the x axis for the 8-nm-thick flake. The black and blue data points are the recorded x - and y -polarized components of the THG power, while the red data points are the measured total THG power. The solid curves are the theoretical fits of the experimental data using Eqs. (3) and (4), which show a good agreement between them. The polarization-dependent THG emission from the merelaniite crystal exhibits an anisotropic two-lobe pattern, where the maximum THG emission occurs with the incident linear polarization, is along the $\pm x$ axis ($\theta = 0^\circ, 180^\circ$). Figures 9(e)–9(h) show the polarization-dependent anisotropic THG emission for other merelaniite flakes with thicknesses of 17, 49, 61, and 121 nm. It is noted that the THG anisotropy ratio $I_x^{(3\omega)}(\theta = 0^\circ)/I_x^{(3\omega)}(\theta = 90^\circ)$ stays almost constant within the range of 1.53 ± 0.11 for all the flakes. The structural anisotropy in merelaniite crystal is further revealed by extracting the relative magnitudes of the elements of the $\chi^{(3)}$ tensor, with the estimated average values of $\chi_{11} : \chi_{12} : \chi_{18} : \chi_{19} : \chi_{21} : \chi_{22} : \chi_{28} : \chi_{29} = 1 : 0.023 : 0.326 : 0.004 : 0.012 : 0.788 : 0.006 : 0.258$, manifesting the intrinsic nature of merelaniite's anisotropic nonlinear optical response. For comparison, Table II lists the extracted relative magnitudes of the elements of the $\chi^{(3)}$ tensor for merelaniite, cylindrite, franckeite, and lengenbachite. It shows that χ_{11} and χ_{22} dominate for all these naturally occurring vdW materials. It is noteworthy that merelaniite has relatively larger values of χ_{18} and χ_{29} compared to cylindrite and lengenbachite, while for franckeite the values of χ_{18} and χ_{29} are much lower than all the others.

Furthermore, the dependence of THG emission as a function of merelaniite flake thickness is explored. Figure 9(i) plots the evolution of the measured average THG power $P^{(3\omega)}$ as a function of the flake thickness d at a pump power of

$P^{(\omega)} = 3.6 \text{ mW}$. The black data points are the measured THG power from five different flakes of thicknesses, ranging from 8 to 121 nm, when the incident linear polarization is along $\theta = 0^\circ$. The THG power increases quadratically up to around 2.11 pW as the flake thickness is increased up to 49 nm, giving the maximum conversion efficiency of 5.86×10^{-10} , and then decays exponentially. The significant attenuation of THG power is attributed to the strong absorption through thick merelaniite flakes. The measured thickness dependence of the THG response can be fitted with an exponentially decaying function $P^{(3\omega)}(d) = Cd^2 \exp(-2d/\delta)$, where $\delta \equiv \frac{\lambda_3}{2\pi k_3}$, C is a constant, and k_3 is the imaginary part of the refractive index at $\lambda_3 = 520 \text{ nm}$, which gives $k_3 = 1.93$. Finally, the effective scalar value of $\chi^{(3)}$ for merelaniite crystal is estimated by using the following relationship [11]:

$$\chi_{\text{eff}}^{(3)} = \left\{ \frac{16\sqrt{n_3^2 + k_3^2} n_1^3 \epsilon_0^2 c^4 f_{\text{rep}}^2 W^4 \tau^2 \left(\frac{\pi}{4 \ln 2}\right)^3 P^{(3\omega)}}{9\omega^2 d^2 P^{(\omega)^3}} \times \left[\frac{(d/\delta)^2}{e^{-2d/\delta} - 2e^{-d/\delta} + 1} \right] e^{2d/\delta} \right\}^{1/2}, \quad (5)$$

where n_1 and n_3 are the real parts of the refractive index of merelaniite at the fundamental wavelength $\lambda_1 = 1560 \text{ nm}$ and the third-harmonic wavelength λ_3 , respectively. The parameters of the fundamental pump laser are given by spot size $W = 1.5 \mu\text{m}$, repetition rate $f_{\text{rep}} = 80 \text{ MHz}$, and pulse width $\tau = 90 \text{ fs}$. By assuming [11] the real part of the refractive index to be $n_1 = n_3 = 3.5$, the $\chi_{\text{eff}}^{(3)}$ value of merelaniite crystal is estimated to be $4.82 \times 10^{-20} \text{ m}^2/\text{V}^2$, which is just slightly smaller than those of the other naturally occurring vdW materials, as shown in Table II.

III. CONCLUSION

We have determined the crystal structure of merelaniite using single-crystal x-ray diffraction. Using the (3 + 2)-dimensional superspace approach, we find that merelaniite's structure is of the cylindrite type, being composed of two C -centered triclinic subsystems: pseudotetragonal (Q layer) of primarily PbS, and pseudo-hexagonal (H layer) that is primarily composed of MoS₂. The layers show large misfit-induced bond-distance modulations and atomic displacements along a single common incommensurate \mathbf{q} wave vector. Within the H layer, Mo atoms occupy octahedral sites. High-resolution scanning transmission electron microscopy shows reasonable agreement with the x-ray diffraction studies. Minor yet visible differences between x-ray and electron diffraction results might be related

to associated differences in sample preparation and the fact that the two isolated single-crystal domains used for the two experiments came from different whiskers and may not be precisely representative of the same bulk. High-resolution scanning transmission electron microscopy further indicates V atoms are concentrated in the *H* layers.

The in-plane structural anisotropy of merelaniite crystal is revealed through angle-resolved polarized Raman spectroscopy. We have also shown that merelaniite flakes can be mechanically exfoliated down to 7 layer-pair thickness. Anisotropic THG response from the exfoliated merelaniite thin flakes is further demonstrated with the extracted anisotropic $\chi^{(3)}$ tensor elements, together with the estimated $\chi_{\text{eff}}^{(3)}$ value of merelaniite crystal, indicating that merelaniite exhibits strong nonlinear optical response similar to other anisotropic nonlinear vdW materials.

Yang *et al.* [51] have described nanoscale layered PbS inclusions 2-, 4-, and 6-atomic layers thick, epitactically aligned and parallel to MoS₂ layers within 2H₁-polytype molybdenite from the Huanglongpu Mo-Pb ore deposit, Qinling orogenic belt, China. They suggest that the PbS layers most likely formed by the diffusion and subsequent exsolution of Pb in Pb-bearing molybdenite due to the different ionic radii of Pb ions as compared to S and Mo ions. While it is unlikely that merelaniite formed by such a mechanism, the observations of Yang *et al.*, together with the cylindrite-group structure of merelaniite, suggest that it may be possible to fabricate a homologous series with different stacking sequences of MoS₂ and PbS layers, and further demonstrate an expanded structure-chemistry space for engineering stable layered materials for potential device applications.

IV. METHODS

A. Materials

Cylindrical merelaniite whiskers in this study were taken from the same specimen as holotype material [30]. They were associated with graphite and occurred on a large alabandite crystal from an unspecified mine in the tanzanite gem mines near Mererani (Merelani), Lelatema Mountains, Simanjoro District, Manyara Region, Tanzania. Separate whiskers were used for each of the different measurements, using the methods described below.

B. Single-crystal x-ray diffraction

A small merelaniite fragment (28 × 25 × 11 μm in size) from the holotype was mounted on a 5-μm-diameter carbon fiber, which was, in turn, attached to a glass rod. Single-crystal x-ray diffraction intensity data were collected with a Bruker D8 Venture Photon 100 CMOS equipped with graphite-monochromatized Mo K α radiation. The detector-to-crystal distance was 70 mm. Data were collected using ω - and φ -scan modes, in 0.5° slices, with an exposure time of 30 s per frame. The data were corrected for Lorentz and polarization factors and absorption using the software package APEX3 [52].

C. Scanning transmission electron microscopy

TEM foils were prepared by embedding a merelaniite whisker in Epofix embedding resin, curing at 60° for 12 h, sectioning with a DiATOME Ultra 35° diamond knife (feed 40 nm, sectioning speed 2 mm/s), and mounting on EMS C-flat™ holey carbon TEM grids. The atomic resolution imaging and x-ray spectroscopy maps were obtained using an FEI Titan Themis aberration-corrected microscope at Michigan Technological University. The imaging and spectroscopic measurements of the sample were performed in scanning mode of the TEM (STEM). The point resolution in STEM mode is 0.8 Å. The microscope was fitted with superX quad detectors for fast mapping with increasing capability to count x rays. For x-ray mapping, typically 25-μs dwell time and 100 picoamps of beam current were used. For both STEM and EDS mapping drift-correction modes were used. STEM and EDS data acquisition and image analysis were performed using Thermo Fisher VELOX.

D. XPS

The XPS spectra were obtained using the Thermo Scientific Nexsa XPS spectroscopy system with a monochromatic Al x-ray source.

E. Optical spectroscopy

The Raman spectra were collected by exciting the sample with a 632.8-nm He-Ne laser using an objective lens and recording the back-reflected light via the same objective lens in a spectrometer (Horiba, iHR 550). The linear polarization of the incident laser beam was adjusted by a linear polarizer and a half-wave plate. An edge filter (Semrock, LP02-633RE-25) was used to reject the laser light. Another linear polarizer in the collection path was used to resolve the parallel component of Raman spectra. The THG signal was collected from the sample excited with a femtosecond laser (wavelength 1560 nm, pulse width 90 fs, repetition rate 80 MHz) using an objective lens. The transmitted THG signal was collected by another objective lens. A short-pass filter was placed in the collection path to block the laser light. The THG signal was then recorded in a spectrometer and a charge-coupled device camera for the analysis.

ACKNOWLEDGMENTS

This research received support from Ministero dell'Istruzione, dell'Università e della Ricerca through the project PRIN 2017 "TEOREM – deciphering geological processes using Terrestrial and Extraterrestrial ORE Minerals," prot. Grant No. 2017AK8C32 (PI: L.B.). The efforts of X.Y. and J.G. were supported by the National Science Foundation Grants No. DMR-1552871 and No. ECCS-1653032. We thank Brian Porter and Eric Bohannon (Missouri University of Science and Technology) for the help in acquiring the XPS and AFM data. The efforts of J.A.J. were supported in part by the Edith D. and E. Wm. Heinrich Mineralogical Research Foundation Trust. We are grateful to Simon Harrison for supplying merelaniite whiskers that became holotype material and from which

samples were selected for this study. We thank Owen P. Mills (Michigan Technological University) and Stacie Kirsch (Electron Microscopy Sciences) for preparation of TEM foils.

L.B., X.Y., and J.A.J. conceptualized this study. X-ray diffraction experiments and analysis were performed by L.B.

Mechanical exfoliation, XPS, AFM analysis, and anisotropic Raman and third-harmonic-generation studies were carried out by A.D., J.G., and X.Y. STEM and EDS studies were conducted by P.M. All authors contributed to writing the manuscript.

- [1] A. K. Geim and I. V. Grigorieva, van der Waals heterostructures, *Nature (London)* **499**, 419 (2013).
- [2] R. Frisenda, Y. Niu, P. Grant, M. Munoz, and A. Castellano-Gomez, Naturally occurring van der Waals materials, *npj 2D Mater. Appl.* **4**, 38 (2020).
- [3] L. Bindi, M. Nespolo, S. V. Krivovichev, G. Chapuis, and C. Biagioni, Producing highly complicated materials. Nature does it better, *Rep. Prog. Phys.* **83**, 106501 (2020).
- [4] M. Velický, P. S. Toth, A. M. Rakowski, A. P. Rooney, A. Kozikov, C. R. Woods, A. Mishchenko, L. Fumagalli, J. Yin, V. Zólyomi, T. Georgiou, S. J. Haigh, K. S. Novoselov, and A. W. Dryfe, Exfoliation of natural van der Waals heterostructures to a single unit cell thickness, *Nat. Commun.* **8**, 14410 (2016).
- [5] A. J. Molina-Mendoza, E. Giovanelli, W. S. Paz, M. A. Niño, J. O. Island, C. Evangeli, L. Aballe, M. Foerster, H. S. J. van der Zant, G. Rubio-Bollinger, N. Agraït, J. J. Palacios, E. M. Pérez, and A. Castellanos-Gomez, Franckeite as a naturally occurring van der Waals heterostructure, *Nat. Commun.* **8**, 14409 (2017).
- [6] K. Ray, A. E. Yore, T. Mou, S. Jha, K. K. H. Smithe, B. Wang, E. Pop, and A. K. M. Newaz, Photoresponse of natural van der Waals heterostructures, *ACS Nano* **11**, 6024 (2017).
- [7] R. Gusmão, Z. Sofer, J. Luxa, and M. Pumera, Layered franckeite and teallite intrinsic heterostructures: Shear exfoliation and electrocatalysis, *J. Mater. Chem. A* **6**, 16590 (2018).
- [8] J. Li, K. Yang, L. Du, J. Yi, J. Huang, J. Zhang, Y. He, B. Huang, L. Miao, C. Zhao, and S. Wen, Nonlinear optical response in natural van der Waals heterostructures, *Adv. Optical Mater.* **8**, 202000382 (2020).
- [9] R. P. N. Tripathi, J. Gao, and X. Yang, Naturally occurring layered mineral franckeite with anisotropic Raman scattering and third-harmonic generation responses, *Sci. Rep.* **11**, 8510 (2021).
- [10] A. Dasgupta, J. Gao, and X. Yang, Natural van der Waals heterostructure cylindrite with highly anisotropic optical responses, *npj 2D Mater. Appl.* **5**, 74 (2021).
- [11] A. Dasgupta, X. Yang, and J. Gao, Naturally occurring van der Waals heterostructure lengenbachite with strong in-plane structural and optical anisotropy, *npj 2D Mater. Appl.* **5**, 88 (2021).
- [12] R. P. N. Tripathi, X. Yang, and J. Gao, Polarization-dependent optical response in natural 2D layered mineral teallite, *Sci. Rep.* **11**, 21895 (2021).
- [13] R. Wadhwa, A. V. Agrawal, and M. Kumar, A strategic review of recent progress, prospects and challenges of MoS₂-based photodetectors, *J. Phys. D: Appl. Phys.* **55**, 063002 (2022).
- [14] A. Taffelli, S. Dirè, A. Quaranta, and L. Pancheri, MoS₂ based photodetectors: A review, *Sensors* **21**, 2758 (2021).
- [15] M. He, D. Winslow, D. Zhang, R. Pandey, and Y. K. Yap, Recent advancement on the optical properties of two-dimensional molybdenum disulfide (MoS₂) thin films, *Photonics* **2**, 288 (2015).
- [16] X. Zhang, X.-F. Qiao, W. Shi, J.-B. Wu, D.-S. Jiang, and P.-H. Tan, Phonon and Raman scattering of two-dimensional transition metal dichalcogenides from monolayer, multilayer to bulk material, *Chem. Soc. Rev.* **44**, 2757 (2015).
- [17] S. Jiménez Sandoval, D. Yang, R. F. Frindt, and J. C. Irwin, Raman study and lattice dynamics of single molecular layers of MoS₂, *Phys. Rev. B* **44**, 3955 (1991).
- [18] F. Wypych and R. Schollhorn, 1T-MoS₂, a new metallic modification of molybdenum-disulfide, *J. Chem. Soc., Chem. Commun.* **19**, 1386 (1992).
- [19] Y. Fang, J. Pan, J. He, R. Luo, D. Wang, X. Che, K. Bu, W. Zhao, P. Liu, G. Mu, H. Zhang, T. Lin, and F. Huang, Structure re-determination and superconductivity observation of bulk 1T MoS₂, *Angew Chem.* **130**, 1246 (2018).
- [20] X. Fan, P. Xu, D. Zhou, Y. Sun, Y. C. Li, Y. M. A. T. Nguyen, M. Terrones, and T. E. Mallouk, Fast and efficient preparation of exfoliated 2H MoS₂ nanosheets by sonication-assisted lithium intercalation and infrared laser-induced 1T to 2H phase reversion, *Nano Lett.* **15**, 5956 (2015).
- [21] D. Kufer, I. Nikitskiy, T. Lasanta, G. Navickaite, F. H. L. Koppens, and G. Konstantatos, Hybrid 2D–0D MoS₂–PbS quantum dot photodetectors, *Adv. Mater.* **27**, 176 (2015).
- [22] D. Kufer, T. Lasanta, M. Bernechea, F. H. L. Koppens, and G. Konstantatos, Interface engineering in hybrid quantum dot–2D phototransistors, *ACS Photonics* **3**, 1324 (2016).
- [23] Y. Wen, L. Yin, P. He, Z. Wang, X. K. Zhang, Q. Wang, T. A. Shifa, K. Xu, F. Wang, X. Zhan, F. Wang, C. Jiang, and J. He, Integrated high-performance infrared phototransistor arrays composed of nonlayered PbS–MoS₂ heterostructures with edge contacts, *Nano Lett.* **16**, 6437 (2016).
- [24] S. Pak, Y. Cho, J. Hong, J. Lee, S. Lee, B. Hou, G.-H. An, Y.-W. Lee, J. E. Jang, H. Im, S. M. Morris, J. I. Sohn, S. N. Cha, and J. M. Kim, Consecutive junction-induced efficient charge separation mechanisms for high-performance MoS₂/Quantum dot phototransistors, *ACS Appl. Mater. Interfaces* **10**, 38264 (2018).
- [25] L. Liu, K. Ye, Z. Yu, Z. Jia, J. Xiang, A. Nie, F. Wen, C. Mu, B. Wang, Y. Li, Y. Gong, and Z. Liu, Photodetection application of one-step synthesized wafer-scale monolayer MoS₂ by chemical vapor deposition, *2D Mater.* **7**, 025020 (2020).
- [26] K. Zhang, S. Feng, S. Kang, Y. Wu, M. Zhang, Q. Wang, Z. Tao, Y. Fan, and W. Lu, Hybrid structure of PbS QDs and vertically-few-layer MoS₂ nanosheets array for broadband photodetector, *Nanotechnology* **32**, 145602 (2021).
- [27] S. R. Tulsani, A. K. Rath, and D. J. Late, 2D-MoS₂ nanosheets as effective hole transport materials for colloidal PbS quantum dot solar cells, *Nanoscale Adv.* **1**, 1387 (2019).
- [28] Q. Wang, Y. Wen, K. Cai, R. Cheng, L. Yin, Y. Zhang, J. Li, Z. Wang, F. Wang, F. Wang, T. A. Shifa, C. Jiang, H. Yang, and J. He, Nonvolatile infrared memory in MoS₂/PbS van der Waals heterostructures, *Sci. Adv.* **4**, eaap7916 (2018).

- [29] X. Xin, Y. Zhang, X. Guan, J. Cao, W. Li, X. Long, and X. Tan, Enhanced performances of PbS quantum-dots-modified MoS₂ composite for NO₂ detection at room temperature, *ACS Appl. Mater. Interfaces* **11**, 9438 (2019).
- [30] J. A. Jaszczak, M. S. Rumsey, L. Bindi, S. A. Hackney, M. A. Wise, C. J. Stanley, and J. Spratt, Merelaniite, Mo₄Pb₄VSb₂, a new molybdenum-essential member of the cylindrite group, from the merelani tanzanite deposit, Lelatema Mountains, Manyara Region, Tanzania, *Minerals* **6**, 115 (2016).
- [31] E. Makovicky and B. G. Hyde, Incommensurate, two-layer structures with complex crystal chemistry: Minerals and related synthetics, *Mater. Sci. Forum* **100-101**, 1 (1992).
- [32] M. Evain, V. Petříček, Y. Moëlo, and C. Maurel, First (3 + 2)-dimensional superspace approach to the structure of levyclaudite-(Sb), a member of the cylindrite-type minerals, *Acta Crystallogr.* **B62**, 775 (2006).
- [33] See Supplemental Material at <http://link.aps.org/supplemental/10.1103/PhysRevMaterials.6.115202> for (a) information about the Crystallographic Information File (.cif) that is available from the authors, (b) high-resolution EDS mapping that includes V, in addition to Pb, Mo, and S, and (c) a comparison of Raman spectra of rolled and unrolled merelaniite whiskers.
- [34] V. Petříček, M. Dušek, and L. Palatinus, Crystallographic computing system JANA2006: General features, *Z. Kristallogr* **229**, 345 (2014).
- [35] B. Schonfeld, J. J. Huang, and S. C. Moss, Anisotropic mean-square displacements (MSD) in single crystals of 2*H*- and 2*R*-MoS₂, *Acta Crystallogr.* **B39**, 404 (1983).
- [36] T. Wagner and A. Schönleber, A non-mathematical introduction to the superspace description of modulated structures, *Acta Crystallogr.* **B65**, 249 (2009).
- [37] P. Hartel, H. Rose, and C. Dinges, Conditions and reasons for incoherent imaging in STEM, *Ultramicroscopy* **63**, 93 (1996).
- [38] S. J. Pennycook, Z-Contrast stem for materials science, *Ultramicroscopy* **30**, 58 (1989).
- [39] S. J. L. Billinge and M. G. Kanatzidis, Beyond crystallography: The study of disorder, nanocrystallinity and crystallographically challenged materials with pair distribution functions, *Chem. Commun.* 749 (2004).
- [40] J.-H. Fan, P. Gao, A.-M. Zhang, B.-R. Zhu, H.-L. Zheng, X.-D. Cui, R. He, and Q.-M. Zhang, Resonance Raman scattering in bulk 2*H*-MX₂ (M = Mo, W; X = W, Se) and monolayer MoS₂, *J. Appl. Phys.* **115**, 053527 (2014).
- [41] G. D. Smith, S. Firth, R. J. H. Clark, and M. Cardona, First- and second-order Raman spectra of galena (PbS), *J. Appl. Phys.* **92**, 4375 (2002).
- [42] R. Parize, T. Cossuet, O. Chaix-Pluchery, H. Roussel, E. Appert, and V. Consonni, In situ analysis of the crystallization process of Sb₂S₃ thin films by Raman scattering and X-ray diffraction, *Mater. Des.* **121**, 1 (2017).
- [43] P. Sereni, M. Musso, P. Knoll, P. Blaha, K. Schwarz, and G. Schmidt, Polarization-dependent Raman characterization of stibnite (Sb₂S₃), *AIP Conf. Proc.* **1267**, 1131 (2010).
- [44] M. Hossain, J. Wu, W. Wen, H. Liu, X. Wang, and L. Xie, Chemical vapor deposition of 2D vanadium disulfide and diselenide and Raman characterization of the phase transitions, *Adv. Mater. Interfaces* **5**, 1800528 (2018).
- [45] Q. Ji, C. Li, J. Wang, J. Niu, Y. Gong, Z. Zhang, Q. Fang, Y. Zhang, J. Shi, L. Liao, and X. Wu, Metallic vanadium disulfide nanosheets as a platform material for multifunctional electrode applications, *Nano Lett.* **17**, 4908 (2017).
- [46] G.-H. Nam, Q. He, X. Wang, Y. Yu, J. Chen, K. Zhang, Z. Yang, D. Hu, Z. Lai, B. Li, Q. Xiong, Q. Zhang, L. Gu, and H. Zhang, In-plane anisotropic properties of 1*T'*-MoS₂ layers, *Adv. Mater.* **31**, 1807764 (2019).
- [47] L. Hart, S. Dale, S. Hoye, J. L. Webb, and D. Wolverson, Rhenium dichalcogenides: Layered semiconductors with two vertical orientations, *Nano Lett.* **16**, 1381 (2016).
- [48] S. Wang and P. R. Buseck, Cylindrite: The relation between its cylindrical shape and modulated structure, *Am. Miner.* **77**, 758 (1992).
- [49] E. Makovicky, V. Petříček, M. Dušek, and D. Topa, Crystal structure of a synthetic tin-selenium representative of the cylindrite structure type, *Am. Miner.* **93**, 1787 (2008).
- [50] X.-I. Yang and S.-W. Xie, Expression of third-order effective nonlinear susceptibility for third-harmonic generation in crystals, *Appl. Opt.* **34**, 6130 (1995).
- [51] Y. Yang, H. He, W. Tan, Q. Tao, J. Yao, H. Xian, S. Li, J. Xi, J. Zhu, J., and H. Xu, Incorporation of incompatible trace elements into molybdenite: Layered PbS precipitates within molybdenite, *Am. Miner.* **107**, 54 (2022).
- [52] Bruker. APEX3; Bruker AXS Inc.: Madison, WI, USA, 2016; Available online: <https://www.bruker.com/products/x-ray-diffraction-and-elemental-analysis/single-crystal-x-ray-diffraction/sc-xrd-software/apex3.html> (accessed on 12 April 2020).